Journal of Alloys and Compounds 832 (2020) 154926

Contents lists available at ScienceDirect

Journal of Alloys and Compounds

journal homepage: http://www.elsevier.com/locate/jalcom

Magnetic properties and magnetic structures in $R_3Ni_2In_4$ (R = Tb–Tm)

S. Baran [a, *], P. Kurzydło [a], Yu. Tyvanchuk [b], A. Hoser [c], A. Szytuła [a]

[a] M. Smoluchowski Institute of Physics, Jagiellonian University, Prof. Stanisława Łojasiewicza 11, PL-30-348, Kraków, Poland
[b] Analytical Chemistry Department, Ivan Franko National University of Lviv, Kyryla and Mephodiya Str. 6, 79005, Lviv, Ukraine
[c] Helmholtz Zentrum Berlin, D-14109, Berlin, Hahn-Meitner-Platz 1, Germany

ARTICLE INFO

Article history:
Received 26 February 2020
Accepted 24 March 2020
Available online 1 April 2020

Keywords:
Intermetallics
Rare earth alloys and compounds
Antiferromagnetism
Frustrated magnetic structure
Neutron diffraction

ABSTRACT

The $R_3Ni_2In_4$ (R = Tb–Tm) ternary indides have been investigated by X-ray and neutron powder diffraction as well as magnetometric measurements. The compounds crystallize in the hexagonal $Lu_3Co_2In_4$-type structure (a lower-symmetry derivative of the ZrNiAl-type one). $Er_3Ni_2In_4$ has been found paramagnetic down to 1.6 K while all other samples order antiferromagnetically below 23.3 K (R = Tb), 9.7 K (R = Dy), 3.3 K (R = Ho) and 3.2 K (R = Tm). The magnetic unit cell in $R_3Ni_2In_4$ (R = Tb, Dy) is doubled along the c-axis with respect to the crystal one (propagation vector $\vec{k} = \left[0, 0, \frac{1}{2}\right]$). The magnetic moments lie in the basal plane and form a "triangular" magnetic structure as often found in geometrically frustrated antiferromagnets. The magnetic order in $Ho_3Ni_2In_4$ consists of two components: a commensurate one which is described above ($\vec{k} = \left[0, 0, \frac{1}{2}\right]$) and an incommensurate one ($\vec{k} = \left[\frac{1}{3}, \frac{1}{3}, k_z\right]$ where $k_z = 0.271(11)$ at 1.6 K). The magnetic moments of the incommensurate component are inclined at a small angle with respect to the basal plane and form a non-collinear magnetic structure. The magnetic structure in $Tm_3Ni_2In_4$ is a commensurate one ($\vec{k} = \left[\frac{1}{3}, \frac{1}{3}, \frac{1}{2}\right]$) with magnetic moments within the basal plane forming a non-collinear "triangular" structure. A determination of magnetic structures is supported by detailed symmetry analysis.

1. Introduction

The rare earth R-Ni-In systems are rich in large number of ternary intermetallic compounds with interesting crystal structure and unique magnetic properties [1]. A significant group of the RNiIn compounds crystallizes in the hexagonal ZrNiAl-type crystal structure [2]. In this structure the rare earth atoms are found to form a triangle network which is a deformed version of the kagome lattice. Magnetic data collected for bulk materials indicate different magnetic properties dependent on rare earth element present. GdNiIn is a ferromagnet with $T_C = 93.5$ K [3,4] or 96 K [5]. Ferromagnetic ground states were claimed also for RNiIn (R = Tb–Er) [5]. However, neutron diffraction studies have confirmed ferromagnetism only in HoNiIn [6] and ErNiIn [6,7] while in RNiIn (R = Tb, Dy) a coexistence of two antiferromagnetic phases (a noncollinear one (NAF) and a phase related to the propagation vector $\vec{k} = \left[\frac{1}{2}, 0, \frac{1}{2}\right]$) has been observed at low temperatures [6]. A modulated incommensurate antiferromagnetic structure has been observed in TmNiIn [8].

Investigation of the R-Ni-In phase diagrams unveils existence of the $RNi_{1-x}In_{1+x}$ solid solutions with x not exceeding 0.35 (R = Gd), 0.50 (R = Tb and Ho) or 0.40 (R = Dy, Er and Tm) [9]. The compounds with x = 0.1 show a decrease of the respective Curie temperatures when compared with those of the stoichiometric 1:1:1 composition (x = 0) [5]. With further increase of x the critical temperatures of magnetic ordering continue to decrease and in case of R = Dy–Er the ferromagnetic order turns into antiferromagnetic one as found for x = 0.25 [5]. Neutron diffraction data collected for the nonstoichiometric $RNi_{1-x}In_{1+x}$ compounds with R = Dy, Ho and Er indicate that the excess In atoms are placed randomly in the 2c site. The structural disorder in the 2c site together with changes in the x-dependent density of states (DOS) at the Fermi level are believed as two main factors leading to the observed complex magnetic ordering [10].

Recently new indides of general composition $R_3Ni_2In_4$ (R = Y, Gd–Tm, Lu) have been discovered [11]. They have been found to crystallize in the hexagonal $Lu_3Co_2In_4$-type structure [12] which is a lower-symmetry derivative of the ZrNiAl-type one. It is worth noting that the $R_3T_2In_4$ family of rare earth intermetallics attracts researchers' interest which is confirmed by late paper on crystal structure and magnetic properties of $R_3T_2In_4$ (R = Dy–Tm; T = Pd,

* Corresponding author.
E-mail address: stanislaw.baran@uj.edu.pl (S. Baran).

https://doi.org/10.1016/j.jallcom.2020.154926

Ir) [13].

This work is a continuation of our systematic studies of physical properties of ternary rare earth-nickel-indides. In this paper we report for the first time magnetic properties, including magnetic structures, of $R_3Ni_2In_4$ (R = Tb–Tm). The compounds have been investigated by means of dc magnetic measurements and neutron diffraction. Based on these data the magnetic properties and magnetic structures of the title compounds have been determined.

2. Experimental details

Polycrystalline samples of $R_3Ni_2In_4$ (R = Tb–Tm) were prepared by arc melting of the constituent elements (purity: 3 N for R and 4 N for Ni and In) under a purified argon atmosphere. In order to assure homogeneity the resulting ingots were sealed in evacuated silica tubes and annealed at 1073 K for 10 days with final quench in cold water. The crystal structure was examined by X-ray powder diffraction which was performed at room temperature using an X'Pert PRO X-ray diffractometer (CuKα radiation).

Magnetic measurements were carried out on a vibrating sample magnetometer (VSM) option of a Quantum Design PPMS platform. Magnetic susceptibility was collected over temperature interval 1.9 K–390 K in applied magnetic fields of 50 Oe (ZFC and FC regimes) and 1 kOe (ZFC regime). Hysteresis loops were taken at 1.9 K in external magnetic field range between −90 kOe and 90 kOe.

Powder neutron diffraction experiments were performed on the E6 ($\lambda = 2.432$ Å) and E9 ($\lambda = 1.798$ Å) diffractometers at the Helmholtz-Zentrum-Berlin. The diffraction patterns were collected at selected temperatures between 1.6 K and 40 K. For measurements the powdered samples were placed in vanadium containers.

All X-ray and neutron diffraction data were refined with the use of the Rietveld-type computer program *FullProf* [14]. For symmetry analysis the *basireps* computer program, which is distributed together with *FullProf*, was utilized [15].

3. Crystal structure

The $R_3Ni_2In_4$ (R = Y, Gd–Tm, Lu) indides have been recently reported by Heying et al. [11] to crystallize in the hexagonal $Lu_3Co_2In_4$-type structure (space group $P\bar{6}$) [12]. Atoms in $R_3Ni_2In_4$ occupy the following Wyckoff sites:

This structure is a lower-symmetry derivative of the well-known hexagonal ZrNiAl-type one (space group $P\bar{6}2m$) [2]. The

3 R at 3*k*:	x_R, y_R, $\frac{1}{2}$
1 Ni_1 at 1*b*:	0, 0, $\frac{1}{2}$
1 Ni_2 at 1*c*:	$\frac{1}{3}$, $\frac{2}{3}$, 0
1 In_1 at 1*e*:	$\frac{2}{3}$, $\frac{1}{3}$, 0
3 In_2 at 3*j*:	x_{In}, y_{In}, 0

lowering of the space group symmetry is related to splitting of the original 2*c* site into two one-fold sites.

X-ray powder diffraction data collected for the investigated samples of $R_3Ni_2In_4$ (R = Tb–Tm) confirmed the $Lu_3Co_2In_4$-type crystal structure with a minor contribution (less than 10 wt %) arising from the RIn_3 [16,17] impurity phase. The determined lattice constants of $R_3Ni_2In_4$ (R = Tb–Tm) were in good agreement with previously reported data [11].

The hexagonal $Lu_3Co_2In_4$-type structure has also been confirmed by powder neutron diffraction data taken in the paramagnetic state. Fig. 1 shows an example of such diffraction pattern, namely the one collected at 5.0 K for $Ho_3Ni_2In_4$. The corresponding values of crystal structure parameters determined from Rietveld refinement are listed in Table 1.

4. Magnetic properties

The magnetic behavior of $R_3Ni_2In_4$ (R = Tb–Tm) is displayed in Fig. 2. Reciprocal magnetic susceptibilities taken at 1 kOe obey the Curie-Weiss law, described by the formula $\chi = \frac{C}{T-\theta_p}$, in wide temperature ranges up to 390 K which was a high temperature limit of the reported experiment. In the equation, *C* refers to Curie constant related to the effective magnetic moment while θ_p is a paramagnetic Curie temperature. Linear least squares fit procedure applied to the experimental data provided effective moments (see Table 2) which are close to the values predicted for the free R^{3+} ions. The fitted lines are shown in red in Fig. 2. All paramagnetic Curie temperatures are negative suggesting that antiferromagnetic interactions are dominant.

At low temperatures (see the upper insets in Fig. 2) maxima typical of transition from antiferro-to paramagnetic state are observed for all compounds except the erbium one (the latter being paramagnetic down to 1.9 K – the low temperature limit of the experiment). The exact values of corresponding Néel temperatures were defined as temperatures at which the maxima in magnetic susceptibility are found. They amount to 23.3 K (R = Tb), 9.7 K (R = Dy), 3.3 K (R = Ho) and 3.2 K (R = Tm) and are marked as vertical dashed lines in the upper insets in Fig. 2. The magnetic susceptibility of $Tb_3Ni_2In_4$ has an additional maximum at 2.3 K (see Fig. 2a) originating from an antiferro-to paramagnetic transition in the Tb_2O_3 impurity phase [18,19]. The existence of small amount of the Er_2O_3 impurity phase in $Er_3Ni_2In_4$ is responsible for observed discrepancy of the ZFC and FC curves below 3.4 K [20] (see Fig. 2d). Nevertheless, the amounts of above mentioned impurity phases are so small that they could not be detected by neither X-ray nor neutron diffraction.

The magnetization curves taken at 1.9 K in external magnetic fields up to 90 kOe do not saturate (see the lower insets in Fig. 2). The magnetic moments found at maximal field applied are significantly smaller than those predicted for the free R^{3+} ions (see

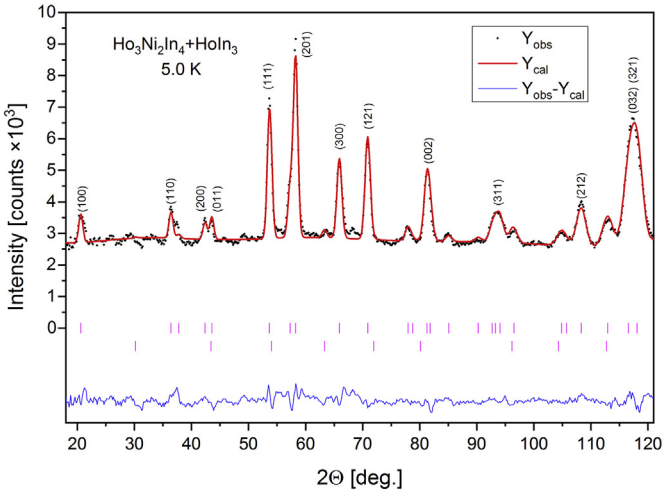

Fig. 1. Neutron diffraction pattern of $Ho_3Ni_2In_4$ collected at 5.0 K (paramagnetic state), its Rietveld fit and the difference plot. The vertical ticks indicate positions of Bragg reflections of the main phase (the upper row) and of the RIn_3 impurity (the bottom row). The data were collected with the use of the E6 diffractometer ($\lambda = 2.432$ Å).

Table 1
Structural parameters of $R_3Ni_2In_4$ (R = Tb–Tm) in the paramagnetic state refined from the neutron diffraction data together with corresponding reliability factors. Temperature of particular measurement is listed in a row marked as "T [K]".

R		Tb	Dy	Ho	Er	Tm
T [K]		30.0	15.4	5.0	5.0	6.3
Crystal structure		$Lu_3Co_2In_4$-type				
Space group		$P\bar{6}$ (No. 174)				
a [Å]		7.729(3)	7.722(2)	7.701(2)	7.687(2)	7.423(2)
c [Å]		3.762(2)	3.7513(9)	3.720(2)	3.699(1)	3.678(2)
V [Å^3]		194.6(2)	193.71(9)	191.0(2)	189.25(8)	175.48(9)
x_{Ho}		0.582(5)	0.581(3)	0.585(6)	0.588(5)	0.582(8)
y_{Ho}		−0.027(5)	−0.026(4)	−0.031(7)	−0.033(6)	−0.038(9)
x_{In_2}		0.240(8)	0.280(20)	0.260(15)	0.265(11)	0.275(16)
y_{In_2}		0.012(12)	0.031(31)	0.019(26)	0.021(20)	0.027(20)
$R_{profile}$ [%]		2.42	2.55	3.16	2.48	3.15
R_{Bragg} [%]		4.74	3.71	4.05	2.57	5.35
χ^2 [%]	5.63	3.70	5.34	2.11	4.55	

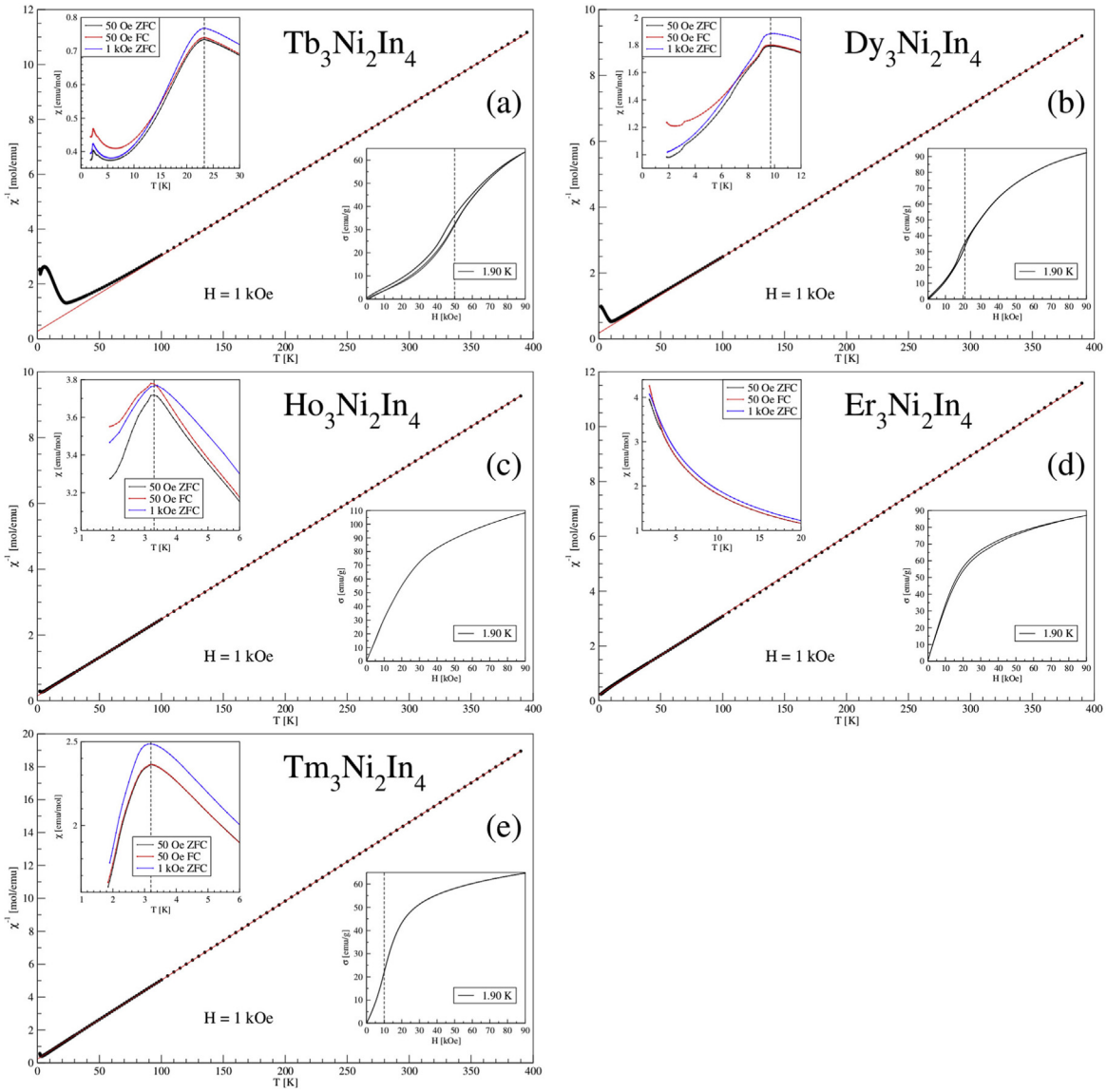

Fig. 2. Reciprocal magnetic susceptibility (circles) together with fitted line representing the Curie-Weiss law for: (a) $Tb_3Ni_2In_4$, (b) $Dy_3Ni_2In_4$, (c) $Ho_3Ni_2In_4$, (d) $Er_3Ni_2In_4$ and (e) $Tm_3Ni_2In_4$. The upper insets show low-temperature behavior of magnetic susceptibility with vertical line referring to a Néel temperature. The bottom insets present a fragment of magnetization loop collected at 1.9 K for fields between 0 and 90 kOe. The vertical line indicates a metamagnetic transition for a virgin curve.

Table 2
Magnetic data of $R_3Ni_2In_4$ (R = Tb–Tm). T_N refers to a Néel temperature, θ_p to a paramagnetic Curie temperature while μ_{eff} to an effective magnetic moment per R^{3+} ion. μ_s is the moment per R^{3+} ion at T = 1.9 K and H = 90 kOe. H_{cr} denotes critical magnetic field as detected from magnetization curve taken at T = 1.9 K. The abbreviation "exp." refers to experimentally determined magnetic moments while the "theor." one refers to the theoretically predicted values for respective R^{3+} ions.

R	T_N [K]	θ_p [K]	μ_{eff} [μ_B]		μ_s [μ_B]		H_{cr}[kOe]
			exp.	theor.	exp.	theor.	
Tb	23.3	−10.1	9.84	9.72	4.00	9.0	50
Dy	9.7	−7.5	10.74	10.65	5.87	10.0	21
Ho	3.3	−6.5	10.67	10.61	6.93	10.0	
Er		−7.1	9.57	9.58	5.62	9.0	
Tm	3.2	−4.8	7.45	7.56	4.19	7.0	10

Table 2). The virgin curves collected for the Tb-, Dy- and Tm-based compounds show metamagnetic transitions at critical fields equal to 50, 21 and 10 kOe, respectively.

The results of magnetometric measurements are summarized in Table 2.

5. Magnetic structure

The results of magnetometric measurements suggest that probably only rare earth atoms possess magnetic moments. There are three such atoms in each crystal unit cell, namely: R_1 at $\left(0.58, 0.97, \frac{1}{2}\right)$, R_2 at $\left(0.03, 0.62, \frac{1}{2}\right)$ and R_3 at $\left(0.38, 0.42, \frac{1}{2}\right)$ – the numbers in parentheses indicate approximate atomic coordinates and slightly depend on chemical composition. In general, each magnetic moment can have its own magnitude and can point at different direction, however, the crystal symmetry imposes constraints on relative directions and magnitudes of magnetic moments occupying particular Wyckoff position. Any periodic magnetic structure can be expressed in terms of its Fourier components. Therefore, a magnetic moment of the *j*th atom located in the *l*th unit cell can be written down as follows:

$$\vec{\mu}_{lj} = \sum_{\vec{k}} \vec{S}_{\vec{k}j} \exp(-2\pi i \vec{k} \cdot \vec{R}_l) \quad (1)$$

where the sum is over all propagation vectors. It is worth noting the $\vec{S}_{\vec{k}j}$ Fourier component is a vector whose components are in general complex numbers. $\vec{R}_l$ is a position vector of the l^{th} unit cell. The theory of representation of space groups, introduced and developed by Bertaut [21] and Izyumov and Syromyatnikov [22], predicts that $\vec{S}_{\vec{k}j}$ Fourier components are linear combination of basis vectors of irreducible representations. The calculations take into account the space group, propagation vector as well as Wyckoff position occupied by magnetic moments.

5.1. $Tb_3Ni_2In_4$ and $Dy_3Ni_2In_4$

The magnetic contributions to neutron diffraction patterns of $Tb_3Ni_2In_4$ and $Dy_3Ni_2In_4$ are very similar to one another. They were obtained by subtracting the paramagnetic data from the patterns taken in the ordered state. The differential pattern of $Tb_3Ni_2In_4$ has been chosen as a representative and is shown in Fig. 3. All Bragg reflections of magnetic origin can be indexed with a propagation vector $\vec{k} = \left[0, 0, \frac{1}{2}\right]$ which corresponds to a magnetic unit cell doubled along the c-axis when compared to the crystal one (see Fig. 4).

Symmetry analysis performed for the $P\bar{6}$ space group, the $\vec{k} = \left[0, 0, \frac{1}{2}\right]$ propagation vector and magnetic moments located at the 3*k* Wyckoff site, shows that this propagation vector is the only

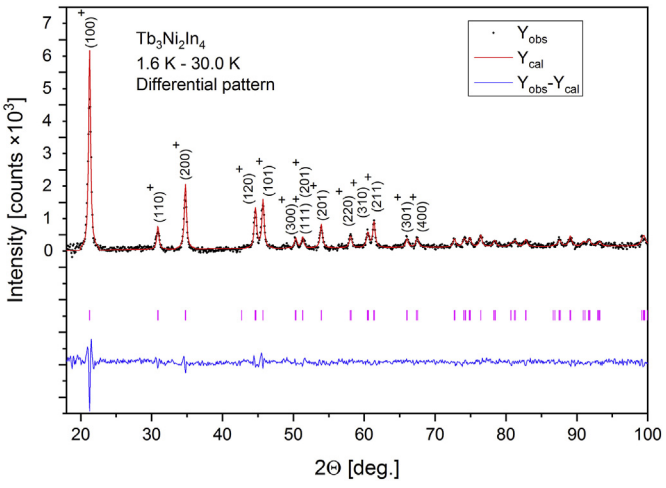

Fig. 3. Differential powder neutron diffraction pattern of $Tb_3Ni_2In_4$ constructed as a difference between the experimental data collected at 1.6 K and 30.0 K. The solid line represents the Rietveld fit. The difference plot is shown in the bottom. The vertical ticks indicate positions of Bragg reflections originating from the magnetic structure formed by the rare earth magnetic moments ($\vec{k} = \left[0, 0, \frac{1}{2}\right]$). The data were collected with the use of the E9 high resolution diffractometer (λ = 1.798 Å).

vector forming a star and all rare earth atoms belong to the same orbit. The theory predicts six 1-dimensional irreducible representations - three of them appearing twice (τ_1, τ_3, τ_5) and another three appearing once (τ_2, τ_4, τ_6). Naming of representations follows the output of the computer program *basireps* [15]. The corresponding basis vectors are listed in Table 3.

The best fit to the experimental data has been obtained for magnetic Fourier components being a linear combination of the basis vectors of τ_1 (marked in bold in Table 3). The corresponding magnetic structure is shown in Fig. 4a while the values of magnetic moments and reliability factors in Table 4. Fig. 4b presents the arrangement of magnetic moments within the basal plane (the moments in the neighbouring (001) planes are coupled antiferromagntically due to the $k_z = \frac{1}{2}$ component of the propagation vector). The magnetic structure is a linear combination of the structures related to the first (see Fig. 4c) and second (see Fig. 4d) set of the τ_1 basis vectors. As the basis vectors of τ_1 have no imaginary components, the magnetic moments on particular rare earth atoms within the reference crystallographic unit cell can be easily calculated using the following formulas: $\vec{\mu}_{R1} = C_1[1,0,0] + C_2[0,1,0]$, $\vec{\mu}_{R2} = C_1[0,1,0] + C_2[-1,-1,0]$ and $\vec{\mu}_{R3} = C_1[-1,-1,0] + C_2[1,0,0]$. The coefficients for $Tb_3Ni_2In_4$, determined from Rietveld refinement of the pattern collected at 1.6 K, equal 7.6 μ_B and 6.7 μ_B for C_1 and C_2, respectively. In $Dy_3Ni_2In_4$, the coefficients have been found to be C_1 = 5.7 μ_B and C_2 = 4.8μ_B, at 1.7 K. As $C_1 \approx C_2$ the magnetic moment directions are close to [1,1,0], [-1,0,0] and [0,-1,0] for the R_1, R_2 and R_3 rare earth atoms, respectively (compare with Fig. 4b).

5.2. $Ho_3Ni_2In_4$

Magnetic contribution to the $Ho_3Ni_2In_4$ diffraction pattern consists of two groups of Bragg reflections (see Fig. 5). The first group corresponds to a commensurate magnetic structure described by a propagation vector $\vec{k} = \left[0, 0, \frac{1}{2}\right]$. Detailed analysis shows that this structure is identical with the one described in section 5.1 for $R_3Ni_2In_4$ (R = Tb, Dy). The C_1 and C_2 coefficients, needed to calculate Ho magnetic moments (see the last paragraph in section 5.1), equal 3.4 μ_B and 3.6 $\mu_B$at 1.6 K while at 3.0 K they have been found to be 1.9 μ_B and 1.8 μ_B, respectively. This group of

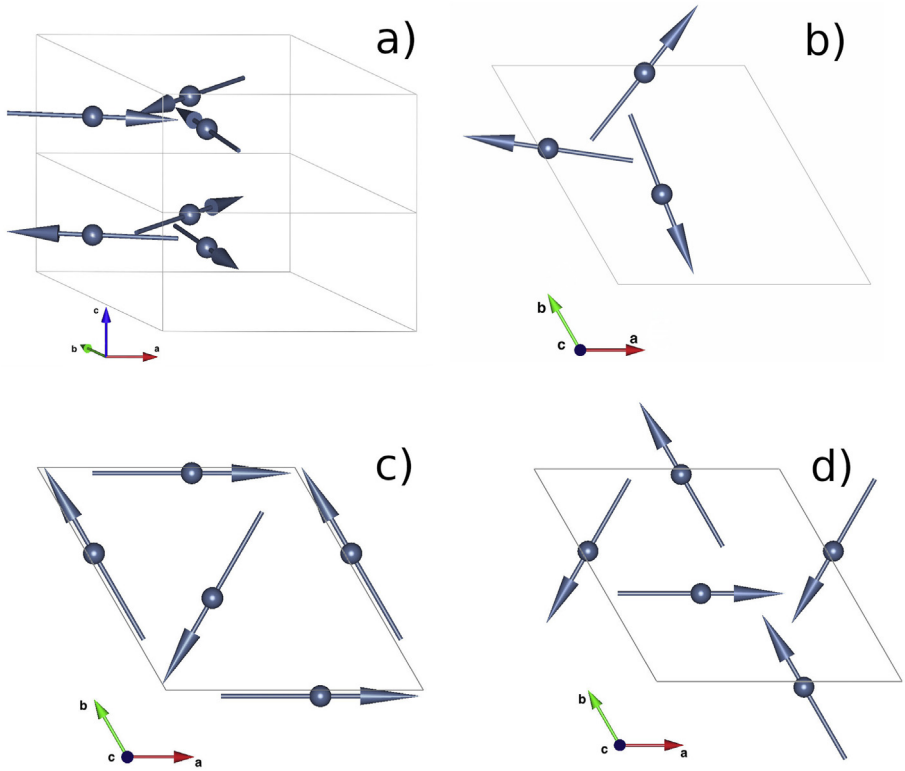

Fig. 4. (a) Magnetic unit cell of the low temperature magnetic structure in $R_3Ni_2In_4$ (R = Tb and Dy) as well as the commensurate component of magnetic structure in $Ho_3Ni_2In_4$. The rare earth magnetic moments in the neighbouring (001) planes are coupled antiferromagnetically due to the $\vec{k} = \left[0, 0, \frac{1}{2}\right]$ propagation vector. (b) Arrangement of magnetic moments within the basal plane. The (c) and (d) insets show arrangement of magnetic moments related to the first and second set of basis vectors of τ_1, respectively (see main text for details).

Table 3
Basis vectors of irreducible representations as calculated for the $P\bar{6}$ space group and the propagation vector $\vec{k} = \left[0,\ 0,\ \frac{1}{2}\right]$. R_1, R_2 and R_3 denote magnetic rare earth atoms. Approximate atomic coordinates are given in parentheses. The set of basis vectors that fits experimental data is marked in bold.

	$R_1\left(0.58,\ 0.97,\ \frac{1}{2}\right)$	$R_2\left(0.03,\ 0.62,\ \frac{1}{2}\right)$	$R_3\left(0.38,\ 0.42,\ \frac{1}{2}\right)$
τ_1	**[1,0,0]**	**[0,1,0]**	**[-1,-1,0]**
	[0,1,0]	**[-1,-1,0]**	**[1,0,0]**
τ_2	[0,0,1]	[0,0,1]	[0,0,1]
τ_3	[1,0,0]	$e^{+\frac{2\pi}{6}i}[0,\ -1,0]$	$e^{-\frac{2\pi}{6}i}[1,1,0]$
	[0,1,0]	$e^{+\frac{2\pi}{6}i}[1,1,0]$	$e^{-\frac{2\pi}{6}i}[-1,0,0]$
τ_4	[0,0,1]	$e^{+\frac{2\pi}{6}i}[0,0,\ -1]$	$e^{-\frac{2\pi}{6}i}[0,0,\ -1]$
τ_5	[1,0,0]	$e^{-\frac{2\pi}{6}i}[0,\ -1,0]$	$e^{+\frac{2\pi}{6}i}[1,1,0]$
	[0,1,0]	$e^{-\frac{2\pi}{6}i}[1,1,0]$	$e^{+\frac{2\pi}{6}i}[-1,0,0]$
τ_6	[0,0,1]	$e^{-\frac{2\pi}{6}i}[0,0,\ -1]$	$e^{+\frac{2\pi}{6}i}[0,0,\ -1]$

reflections decreases monotonically with increasing temperature.

The second group of Bragg reflections of magnetic origin is related to an incommensurate magnetic structure described by a propagation vector $\vec{k} = \left[\frac{1}{3}, \frac{1}{3}, k_z\right]$ where $k_z = 0.271(11)$ at 1.6 K. In contrast to the first group, the second group increases with increasing temperature, reaching its maximum in intensity above 3 K and then disappears. Symmetry analysis shows that the vector $\left[\frac{1}{3}, \frac{1}{3}, k_z\right]$ forms a star together with $\left[\frac{1}{3}, \frac{1}{3}, -k_z\right]$ while all rare earth magnetic moments occupying the 3*k* Wyckoff site belong to one orbit. The theory predicts three 1-dimensional irreducible representations each of them appearing three times. The basis vectors of the irreducible representations are listed in Table 5. The best fit to the experimental data is found for Fourier components being a linear combination of the basis vectors of τ_3. The following formulas are used to calculate the Fourier components of magnetic moments related to Ho atoms within the crystallographic unit cell: $\vec{S}_{\vec{k}1} = \frac{1}{2}e^{-2\pi i\left(\frac{1}{6}+\varphi\right)}(C_1[1,0,0] + C_2[0,1,0] + C_3[0,0,1])$, $\vec{S}_{\vec{k}2} = \frac{1}{2}e^{-2\pi i\left(\frac{1}{6}+\varphi\right)}(C_1[0,-1,0] + C_2[1,1,0] + C_3[0,0,-1])$ and $\vec{S}_{\vec{k}3} = \frac{1}{2}e^{-2\pi i\left(\frac{1}{6}+\varphi\right)}(C_1[1,1,0] + C_2[-1,0,0] + C_3[0,0,-1])$. The 1, 2 and 3 indices refer to Ho_1, Ho_2 and Ho_3, respectively, while φ is the "global magnetic phase factor" as the same value is applied to all Fourier components. In case of incommensurate magnetic structures, the φ parameter has no physical meaning as it is related only to the choice of origin of the coordinate system. Thus φ was fixed to zero during refinement. The Rietveld refinement has yielded the following values of the coefficients: $C_1 = 0.1\ \mu_B$, $C_2 = 0.3\ \mu_B$ and $C_3 = -0.3\ \mu_B$ at 1.6 K while at 3.0 K $C_1 = 2.1\ \mu_B$, $C_2 = 1.8\ \mu_B$ and $C_3 = -0.1\ \mu_B$. As the magnetic moments have only real components (no imaginary part), according to equation (1), both $\vec{S}_{\vec{k}}$ and $\vec{S}_{-\vec{k}}$ Fourier components have to be taken into account while calculating magnetic moments. Thus the magnetic moments in the reference crystallographic unit cell are given by: $\vec{\mu}_{Ho1} = \vec{S}_{\vec{k}1} + \vec{S}_{-\vec{k}1} = C_1[1,0,0] + C_2[0,1,0] + C_3[0,0,1]$, $\vec{\mu}_{Ho2} = \vec{S}_{\vec{k}2} + \vec{S}_{-\vec{k}2} = \frac{1}{2}(C_1[0,-1,0] + C_2[1,1,0] + C_3[0,0,-1])$ and $\vec{\mu}_{Ho3} = \vec{S}_{\vec{k}3} + \vec{S}_{-\vec{k}3} = \frac{1}{2}(C_1[1,1,0] + C_2[-1,0,0] + C_3[0,0,-1])$ (assuming $\varphi = 0$). The moments in any other crystallographic unit cell can be calculated using equation (1). As $C_1 \approx C_2$ and $|C_3| \ll C_1$ at 3.0 K, the Ho magnetic moments are close to the basal plane (in fact

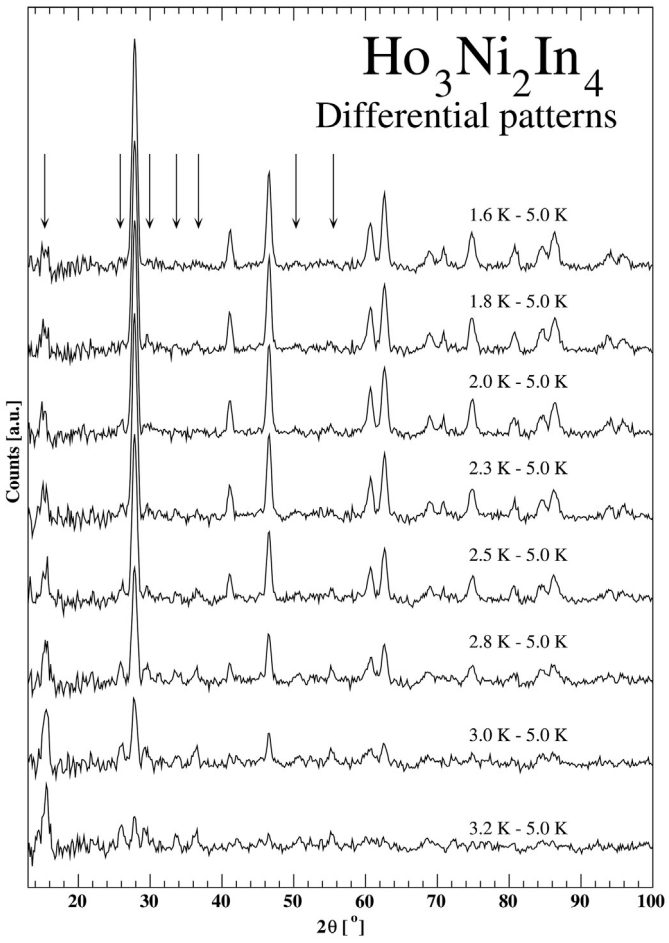

Fig. 5. Thermal evolution of magnetic contribution to the $Ho_3Ni_2In_4$ powder neutron diffraction pattern. The most intense Bragg reflections originate from commensurate magnetic structure related to a propagation vector $\vec{k} = \left[0,0,\frac{1}{2}\right]$ (the same magnetic structure as found for $R_3Ni_2In_4$, where R = Tb and Dy). The second group reflections originates from an incommensurate magnetic structure related to $\vec{k} = \left[\frac{1}{3},\frac{1}{3},k_z\right]$ (the exact values of k_z are listed in Table 4). Positions of the main reflections coming from the incommensurate ordering have been marked by arrows. The data were collected with the use of the E6 diffractometer ($\lambda = 2.432$ Å).

they are inclined at an angle of about 12°). When projected on the basal plane the magnetic moments directions are close to [1,1,0], [1,0,0] and [0,1,0] for Ho_1, Ho_2 and Ho_3, respectively. A fragment of the incommensurate component of the $Ho_3Ni_2In_4$ magnetic structure, as determined from Rietveld refinement of the pattern collected at 3.0 K, is presented in Fig. 6.

The low temperature differential neutron diffraction patterns of $Ho_3Ni_2In_4$ together with Rietveld fits are shown in Fig. 7. The parameters characterizing the magnetic structure of $Ho_3Ni_2In_4$ (the commensurate and incommensurate components) are summarized in Table 4.

5.3. $Er_3Ni_2In_4$

$Er_3Ni_2In_4$ shows no signs of long-range magnetic ordering down to 1.6 K as presented in Fig. 8 – a differential pattern constructed as a difference between the patterns collected at 1.6 K and 5.0 K does not contain magnetic contribution in form of Bragg reflections. A wide bump around $2\theta = 30^o$ can be attributed to short-range magnetic ordering.

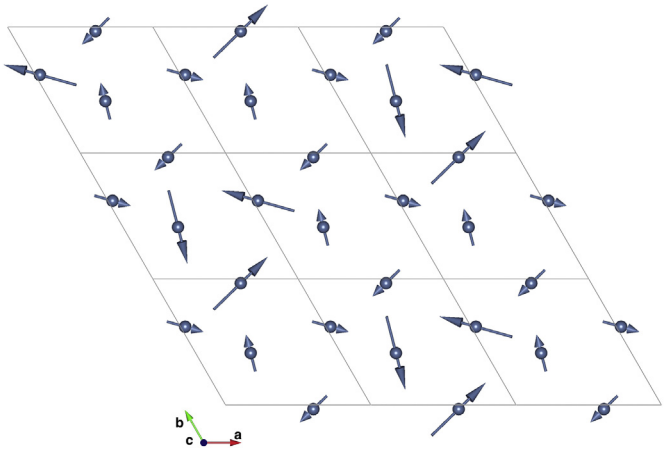

Fig. 6. Incommensurate component ($\vec{k} = \left[\frac{1}{3},\frac{1}{3},k_z\right]$; the exact values of k_z are listed in Table 4) of the $Ho_3Ni_2In_4$ magnetic structure projected into the basal plane. The figure is based on results of refinement of diffraction data collected at 3.0 K. As the structure is incommensurate a magnetic unit cell cannot be defined. Thus the presented area gives only a general idea how the structure looks like. The same structure is obtained by taking into account either the basis vectors of the irreducible representation τ_1 or those of τ_3 (see main text for details).

5.4. $Tm_3Ni_2In_4$

Magnetic contribution to the $Tm_3Ni_2In_4$ neutron diffraction pattern is different from those described above – it corresponds to a commensurate magnetic structure related to a propagation vector $\vec{k} = \left[\frac{1}{3},\frac{1}{3},\frac{1}{2}\right]$ (see Fig. 9). Symmetry analysis shows that this vector forms a star together with $\left[\frac{1}{3},-\frac{2}{3},\frac{1}{2}\right]$, $\left[\frac{1}{3},\frac{1}{3},-\frac{1}{2}\right]$, $\left[-\frac{2}{3},\frac{1}{3},\frac{1}{2}\right]$, $\left[\frac{1}{3},-\frac{2}{3},-\frac{1}{2}\right]$ and $\left[-\frac{2}{3},\frac{1}{3},-\frac{1}{2}\right]$. All magnetic moments occupying the 3*k* Wyckoff site belong to one orbit. The theory predicts six 1-dimensional irreducible representations – three of them appearing twice (τ_1,τ_3,τ_5) and another three appearing once (τ_2,τ_4,τ_6). The corresponding basis vectors are listed in Table 6.

The best fit has been obtained for Fourier components taken as a linear combination of the basis vectors of τ_3 leading to the magnetic structure with magnetic moments confined to the basal plane. The corresponding Fourier components are given by: $\vec{S}_{\vec{k}1} = \frac{1}{2}e^{-2\pi i\varphi}(C_1[1,0,0] + C_2[0,1,0])$, $\vec{S}_{\vec{k}2} = \frac{1}{2}e^{-2\pi i\varphi}(C_1[0,1,0] + C_2[-1,-1,0])$ and $\vec{S}_{\vec{k}3} = \frac{1}{2}e^{-2\pi i\varphi}(C_1[-1,-1,0] + C_2[1,0,0])$. Magnetic moments in the reference crystallographic unit cell are therefore expressed as: $\vec{\mu}_{Tm1} = \vec{S}_{\vec{k}1} + \vec{S}_{-\vec{k}1} = \cos\varphi(C_1[1,0,0] + C_2[0,1,0])$, $\vec{\mu}_{Tm2} = \vec{S}_{\vec{k}2} + \vec{S}_{-\vec{k}2} = \cos\varphi(C_1[0,1,0] + C_2[-1,-1,0])$ and $\vec{\mu}_{Tm3} = \vec{S}_{\vec{k}3} + \vec{S}_{-\vec{k}3} = \cos\varphi(C_1[-1,-1,0] + C_2[1,0,0])$. As the magnetic unit cell is 18 times bigger than the crystallographic one ($\vec{k} = \left[\frac{1}{3},\frac{1}{3},\frac{1}{2}\right]$), in order to calculate magnetic moments in other parts of the magnetic unit cell equation 1 has to be used.

The C_1 and C_2 parameters, as derived form Rietveld refinement of the pattern taken at 1.6 K equal −2.2 μ_B and 4.0 μ_B, respectively. The results of refinement together with reliability factors are summarized in Table 4. As $C_1 \approx -\frac{1}{2}C_2$ the directions of magnetic moments are close to [-1,2,0], [-2,-3,0] and [3,1,0] for Tm_1, Tm_2 and Tm_3, respectively. It has to be mentioned that in case of the magnetic structures commensurate with the crystal ones, the value of "global magnetic phase factor" parameter φ is important as it influences the magnitudes of magnetic moments in different locations at the magnetic unit cell. φ cannot be determined from Rietveld refinement as it does not affect the calculated diffraction pattern. Thus it has to be chosen arbitrarily. It is worth noting that although the corresponding magnetic structure is a commensurate one there is no solution with all rare earth magnetic moments of

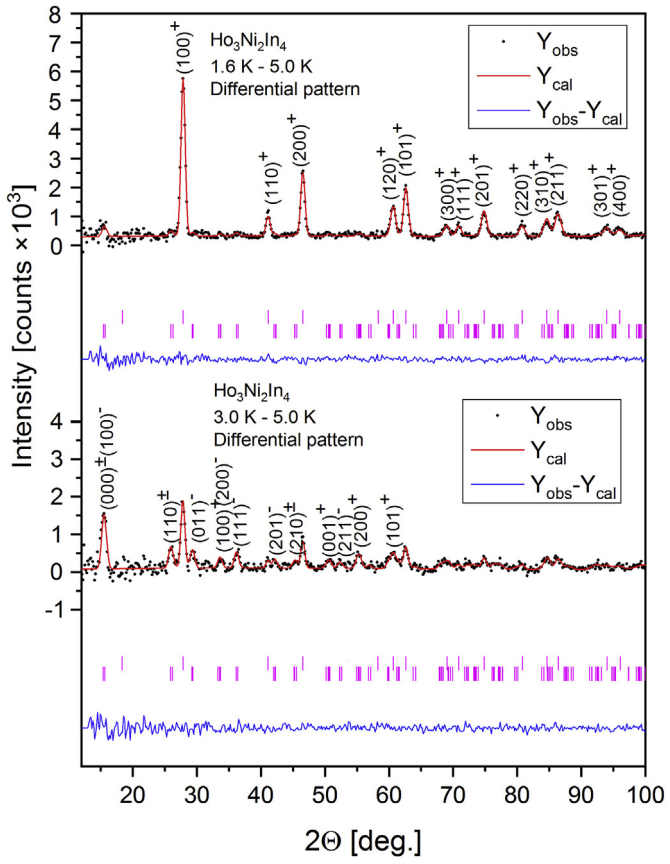

Fig. 7. Differential powder neutron diffraction patterns of $Ho_3Ni_2In_4$ constructed as a difference between the experimental data collected at low temperature (1.6 K or 3.0 K) and at 5.0 K (paramagnetic state). The red solid line represents the Rietveld fit while the blue one is for the difference plot. The upper row of vertical ticks indicates positions of Bragg reflections originating from the commensurate component ($\vec{k} = \left[0, 0, \frac{1}{2}\right]$) of the $Ho_3Ni_2In_4$ magnetic structure. The second row is related to the incommensurate component ($\vec{k} = \left[\frac{1}{3}, \frac{1}{3}, k_z\right]$; the exact values of k_z are listed in Table 4). The Miller indices in the upper part refer to the commensurate component of the magnetic structure while those in the bottom part to the incommensurate one. The data were collected with the use of the E6 diffractometer ($\lambda = 2.432$ Å). (For interpretation of the references to colour in this figure legend, the reader is referred to the Web version of this article.)

Table 5
Basis vectors of irreducible representations as calculated for the $P\bar{6}$ space group and the propagation vector $\vec{k} = \left[\frac{1}{3}, \frac{1}{3}, k_z\right]$ ($k_z \approx 0.27$). R_1, R_2 and R_3 denote magnetic rare earth atoms. Approximate atomic coordinates are given in parentheses. The set of basis vectors that fits experimental data is marked in bold (see main text for details).

	$R_1\left(0.58, 0.97, \frac{1}{2}\right)$	$R_2\left(0.03, 0.62, \frac{1}{2}\right)$	$R_3\left(0.38, 0.42, \frac{1}{2}\right)$
τ_1	[1, 0, 0]	$e^{-\frac{2\pi}{6}i}$[0, −1, 0]	$e^{+\frac{2\pi}{6}i}$[1, 1, 0]
	[0, 1, 0]	$e^{-\frac{2\pi}{6}i}$[1, 1, 0]	$e^{+\frac{2\pi}{6}i}$[−1, 0, 0]
	[0, 0, 1]	$e^{-\frac{2\pi}{6}i}$[0, 0, −1]	$e^{+\frac{2\pi}{6}i}$[0, 0, −1]
τ_2	[1,0,0]	[0,1,0]	[-1,-1,0]
	[0,1,0]	[-1,-1,0]	[1,0,0]
	[0,0,1]	[0,0,1]	[0,0,1]
τ_3	**[1, 0, 0]**	$\mathbf{e^{+\frac{2\pi}{6}i}[0, -1, 0]}$	$\mathbf{e^{-\frac{2\pi}{6}i}[1, 1, 0]}$
	[0, 1, 0]	$\mathbf{e^{+\frac{2\pi}{6}i}[1, 1, 0]}$	$\mathbf{e^{-\frac{2\pi}{6}i}[-1, 0, 0]}$
	[0, 0, 1]	$\mathbf{e^{+\frac{2\pi}{6}i}[0, 0, -1]}$	$\mathbf{e^{-\frac{2\pi}{6}i}[0, 0, -1]}$

the same magnitude. In Fig. 10 an exemplary structure with two values of magnetic moments (either 5.4 μ_B or 2.7 μ_B), obtained while assuming $\varphi = \frac{1}{4}$ (in the units of 2π), is shown. However, one should take into account that other solutions, like for example those with zero magnetic moment on selected rare earth ions, are still valid from mathematical point of view.

6. Discussion

The results of X-ray and neutron powder diffraction confirm that the $R_3Ni_2In_4$ (R = Tb–Tm) ternary indides crystallize in the hexagonal $Lu_3Co_2In_4$-type structure [12]. In this structure the atomic framework forms two types of basal plane layers: with and without rare earth atoms, i.e. (3R + Ni) for z = 0.5 and (4In + Ni) for z = 0. The R atoms, occupying the 3*k* Wyckoff site, form a triangular structure which is a deformed kagome lattice. Such an arrangement of atoms carrying magnetic moments leads, in case of antiferromagnetic interactions, to geometrically frustrated magnetic

Table 4
Parameters of magnetic structures in $R_3Ni_2In_4$ (R = Tb–Tm) as determined from powder neutron diffraction. *T* denotes temperature at which the data have been collected. $\vec{k}$ refers to a propagation vector. μ is a magnetic moment (used to describe magnetic structures having all magnetic moments of the same magnitude) while μ_A is an amplitude of modulation of magnetic moment (used to describe incommensurate magnetic structures as well as commensurate magnetic structures having magnetic moments of different magnitudes). *DMM* refers to the direction of magnetic moment. The table contains also the following residuals characterizing fit quality: $R_{profile}$, $R_{magnetic}$ and χ^2. For $Ho_3Ni_2In_4$ the results of refinements at two different temperatures are listed in order to show thermal evolution of the corresponding magnetic structure.

R	*T*[K]	$\vec{k}$	μ [μ_B]	μ_A [μ_B]	DMM	$R_{profile}$	$R_{magnetic}$	χ^2
Tb	1.6	$\left[0, 0, \frac{1}{2}\right]$	7.1		⊥ c	2.56	10.8	1.92
Dy	1.7	$\left[0, 0, \frac{1}{2}\right]$	5.4		⊥ c	2.55	15.8	3.59
Ho	1.6	$\left[0, 0, \frac{1}{2}\right]$	3.5		⊥ c	2.52	6.71	3.03
		$\left[\frac{1}{3}, \frac{1}{3}, 0.271(11)\right]$		0.5	⊥ c[a]		35.6	
Ho	3.0	$\left[0, 0, \frac{1}{2}\right]$	1.9		⊥ c	2.24	9.14	2.67
		$\left[\frac{1}{3}, \frac{1}{3}, 0.278(10)\right]$		3.7	⊥ c[a]		12.9	
Er	No magnetic ordering detected down to 1.6 K.							
Tm	2.0	$\left[\frac{1}{3}, \frac{1}{3}, \frac{1}{2}\right]$		5.4	⊥ c	2.43	12.4	2.61

[a] In case of the incommensurate magnetic order in $Ho_3Ni_2In_4$ the best fit has been obtained for magnetic moments having a small component along the c-axis. The moments form an angle of about 12° with the ab-plane. Such a magnetic structure is allowed by symmetry (see Table 5).

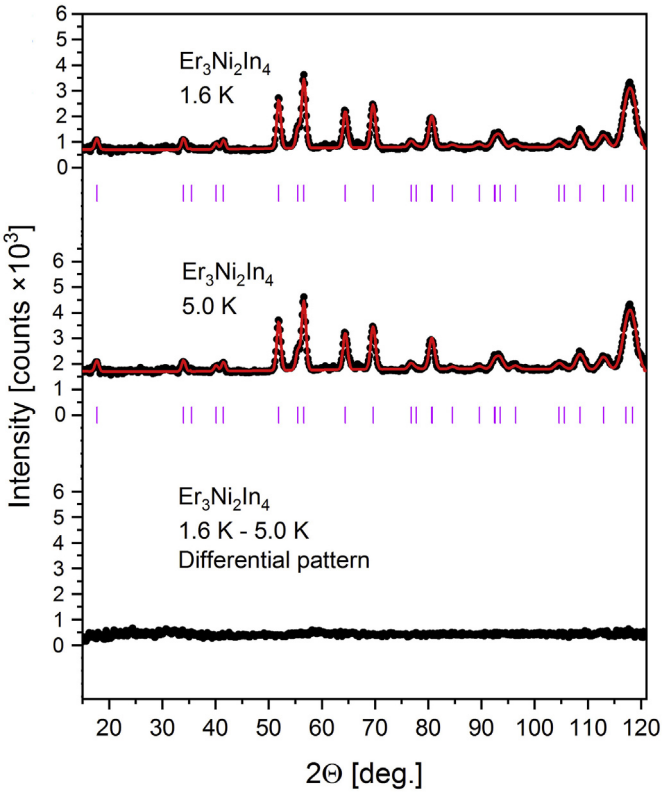

Fig. 8. Powder neutron diffraction patterns of $Er_3Ni_2In_4$ taken at 1.6 K and 5.0 K together with a differential pattern (at the bottom). The red lines show the results of Rietveld refinement of a pure nuclear phase (no magnetic contribution) while vertical ticks indicate positions of corresponding Bragg reflections. The data were collected with the use of the E6 diffractometer ($\lambda = 2.432$ Å). (For interpretation of the references to colour in this figure legend, the reader is referred to the Web version of this article.)

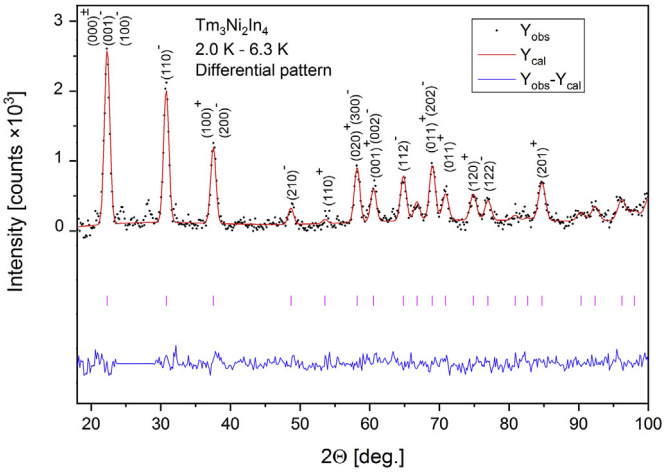

Fig. 9. Differential powder neutron diffraction pattern of $Tm_3Ni_2In_4$ constructed as a difference between the experimental data collected at 2.0 K and 6.3 K. The solid line represents the Rietveld fit. The difference plot is shown in the bottom. The vertical ticks indicate positions of Bragg reflections originating from the magnetic structure formed by the rare earth magnetic moments ($\vec{k} = \left[\frac{1}{3}, \frac{1}{3}, \frac{1}{2}\right]$). The two weak magnetic reflections at 24.5° and 28.1° originate from an unidentified impurity. Thus the angle range from 24° to 29° was excluded from refinement. The data were collected with the use of the E6 diffractometer ($\lambda = 2.432$ Å).

Table 6
Basis vectors of irreducible representations as calculated for the $P\bar{6}$ space group and the propagation vector $\vec{k} = \left[\frac{1}{3}, \frac{1}{3}, \frac{1}{2}\right]$. R_1, R_2 and R_3 denote magnetic rare earth atoms. Approximate atomic coordinates are given in parentheses. The set of basis vectors that fits experimental data is marked in bold.

	$R_1\left(0.58, 0.97, \frac{1}{2}\right)$	$R_2\left(0.03, 0.62, \frac{1}{2}\right)$	$R_3\left(0.38, 0.42, \frac{1}{2}\right)$
τ_1	[1, 0, 0]	$e^{-\frac{2\pi}{6}i}$ [0, −1, 0]	$e^{+\frac{2\pi}{6}i}$ [1, 1, 0]
	[0, 1, 0]	$e^{-\frac{2\pi}{6}i}$ [1, 1, 0]	$e^{+\frac{2\pi}{6}i}$ [−1, 0, 0]
τ_2	[0,0,1]	$e^{-\frac{2\pi}{6}i}$ [0, 0, −1]	$e^{+\frac{2\pi}{6}i}$ [0, 0, −1]
τ_3	**[1, 0, 0]**	**[0, 1, 0]**	**[−1, −1, 0]**
	[0, 1, 0]	**[−1, −1, 0]**	**[1, 0, 0]**
τ_4	[0,0,1]	[0,0,1]	[0,0,1]
τ_5	[1, 0, 0]	$e^{+\frac{2\pi}{6}i}$ [0, −1, 0]	$e^{-\frac{2\pi}{6}i}$ [1, 1, 0]
	[0, 1, 0]	$e^{+\frac{2\pi}{6}i}$ [1, 1, 0]	$e^{-\frac{2\pi}{6}i}$ [−1, 0, 0]
τ_6	[0,0,1]	$e^{+\frac{2\pi}{6}i}$ [0, 0, −1]	$e^{-\frac{2\pi}{6}i}$ [0, 0, −1]

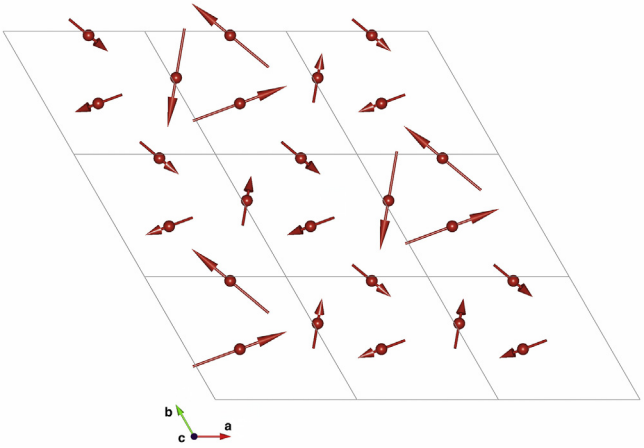

Fig. 10. Low temperature magnetic structure in $Tm_3Ni_2In_4$. Only half of the magnetic unit cell is shown. The rare earth magnetic moments in the neighbouring (001) planes are coupled antiferromagnetically due to the $\vec{k} = \left[\frac{1}{3}, \frac{1}{3}, \frac{1}{2}\right]$ propagation vector.

structures. The determined lattice constants as well as atomic positional parameters are in good agreement with the previously reported X-ray data [11].

Magnetic susceptibility vs. temperature dependences indicate an antiferromagnetic ordering at low temperatures in all title compounds except $Er_3Ni_2In_4$ which is found paramagnetic down to 1.9 K (see Fig. 2). The Néel temperatures ranges from 3.2 K (R = Tm) up to 23.3 K (R = Tb). Reciprocal magnetic susceptibilities obey the Curie-Weiss law in a broad temperature range. Deviations from linearity are found only at low temperatures in vicinities of the respective Néel points. All paramagnetic Curie temperatures are negative indicating a dominant contribution from antiferromagnetic interactions. The effective magnetic moments are close to the values predicted for free R^{3+} ions. The discrepancies not exceeding 1.5% can be attributed to the sum of systematic errors of magnetic susceptibility and sample mass measurements. It is worth noting that similar antiferromagnetic properties were found in $R_3Ir_2In_4$ (R = Dy, Tm). The Néel temperature of $Dy_3Ir_2In_4$ equals 13.6 K while that of $Tm_3Ir_2In_4$ was found to be 5.4 K [13].

The results of neutron diffraction confirm above mentioned magnetometric data. No long-range magnetic order is found in $Er_3Ni_2In_4$ down to 1.6 K while in all other remaining compounds an

antiferromagnetic order is found at low temperatures. In the latter case a good agreement with experimental data can be obtained assuming that only rare earth atoms carry magnetic moments.

A significant change in magnetic structure is found with increase of the number of $4f$ electrons. For R = Tb and Dy a simple antiferromagnetic structure with the magnetic unit cell doubled when compared with the crystal one is found ($\vec{k} = \left[0,0,\frac{1}{2}\right]$). The rare earth magnetic moments lie in the basal plane and show a 'triangular' arrangement which is characteristic of geometrically frustrated systems where magnetic moments form the (distorted) kagome lattice. In $Ho_3Ni_2In_4$ a coexistence of the mentioned above commensurate antiferromagnetic structure ($\vec{k} = \left[0,0,\frac{1}{2}\right]$) with the incommensurate one ($\vec{k} = \left[\frac{1}{3},\frac{1}{3},k_z\right]$ where $k_z \approx 0.27$) is observed. It is worth noting that although the latter structure has a dominant inplane component of magnetic moment the refinement suggests a presence of a small component perpendicular to the basal plane. Nevertheless, such a result is allowed by symmetry (see Table 5). No magnetic ordering has been discovered in $Er_3Ni_2In_4$ down to 1.6 K. In $Tm_3Ni_2In_4$ again a commensurate antiferromagnetic structure is found, however, it is different from the one observed for the lighter rare earth elements. The magnetic unit cell is 18 times larger than the crystal one and corresponds to a propagation vector $\vec{k} = \left[\frac{1}{3},\frac{1}{3},\frac{1}{2}\right]$. The thulium magnetic moments lie in the basal plane.

The determined arrangement of magnetic moments within the basal plane can be compared with theoretical predictions reported by Gondek and Szytuła [23]. The authors considered magnetic moments occupying a distorted kagome lattice which is found in rare earth intermetallics crystallizing in the ZrNiAl-type hexagonal structure. The exchange interactions with the nearest (J_1) and the second nearest (J_2) neighbours as well as the Dzialoshinsky–Moriya interaction have been taken into account. It has been found that non-zero Dzialoshinsky–Moriya interaction leads to appearance of magnetic structures described by a propagation vector of general formula $[k_x, k_x]$ where $0 < k_x < \frac{1}{3}$. This is not the case of magnetic structures observed in $R_3Ni_2In_4$ where an inplane antiferromagnetic ordering is described by either $[0,0]$ (R = Tb, Dy and the commensurate component of Ho) or $\left[\frac{1}{3},\frac{1}{3}\right]$ (R = Ho (the incommensurate component) and Tm). These two mentioned propagation vectors appear in the magnetic phase diagram determined in absence of the Dzialoshinsky–Moriya interaction (see Fig. 1 in [23]), namely, the antiferromagnetic order (AF1-type) related to $[0,0]$ is obtained for $J_1 < 0$ and $J_2 < 0$ while that related to $\left[\frac{1}{3},\frac{1}{3}\right]$ (AF2-type) for $J_1 < 0$ and $J_2 > 0$. Thus increasing number of the $4f$ electrons in $R_3Ni_2In_4$ is correlated with a change in sign of the J_2 exchange integral from negative to positive one.

Propagation vectors describing the magnetic order in $R_3Ni_2In_4$ possess a non-zero k_z component characteristic of either antiferromagnetic coupling between neighbouring (001) planes ($k_z = \frac{1}{2}$) or a sine-type modulation along the c-axis ($k_z \approx 0.27$).

Declaration of competing interest

The authors declare that they have no known competing financial interests or personal relationships that could have appeared to influence the work reported in this paper.

Acknowledgements

Kind hospitality and financial support extended to two of us (S. B. and A. S.) by the Helmholtz- Zentrum Berlin für Materialien und Energie (HZB) is gratefully acknowledged.

The magnetic measurements were carried out with the equipment purchased thanks to the financial support of the European Regional Development Fund in the framework of the Polish Innovation Economy Operational Program (contract no. POIG.02.01.00-12-023/08).

References

[1] Ya Kalychak, V. Zaremba, R. Pöttgen, M. Lukachuk, R.-D. Hoffmann, in: K.A. Gschneider, J.C.G. Bunzli, V.K. Pecharsky (Eds.), Handbook on the Physics and Chemistry of Rare Earths, vol. 34, Elsevier, Amsterdam, 2004, pp. 1–133, ch. 218.
[2] R. Ferro, R. Marazza, G. Rambaldi, Z. Metallkd. 65 (1974) 37–39.
[3] F. Merlo, M.L. Fornasini, S. Cirafici, F. Canepa, J. Alloys Compd. 267 (1998). L12–L13.
[4] F. Canepa, M. Napoletano, A. Palenzona, F. Merlo, S. Cirafici, J. Phys. D Appl. Phys. 32 (1999) 2721–2725.
[5] Yu B. Tyvanchuk, Ya M. Kalychak, Ł. Gondek, M. Rams, A. Szytuła, Z. Tomkowicz, J. Magn. Magn Mater. 277 (2004) 368–378.
[6] Ł. Gondek, A. Szytula, S. Baran, J. Hernandez-Velasco, J. Magn. Magn Mater. (2004) e443–e444, 272–276.
[7] Ł. Gondek, A. Szytuła, B. Penc, J. Hernandez-Velasco, A. Zygmunt, J. Magn. Magn Mater. 262 (2003) L177–L180.
[8] S. Baran, D. Kaczorowski, A. Arulraj, B. Penc, A. Szytuła, J. Magn. Magn Mater. 323 (2011) 833–837.
[9] Ya M. Kalychak, V.I. Zaremba, Yu B. Tyvachuk, Proc. VIth Int. Conf. Crystal Chem. Intermetallic Compounds, Lviv, Ukraine, September 26–29, 1995, p. 77.
[10] Ł. Gondek, A. Szytuła, S. Baran, M. Rams, J. Hernandez-Velasco, Yu Tyvanchuk, J. Magn. Magn Mater. 278 (2004) 392–396.
[11] B. Heying, O. Niehaus, U. Ch Rodewald, R. Pöttgen, Z. Naturforsch. 71b (2016) 1261–1267.
[12] V.I. Zaremba, Y.M. Kalychak, P Yu Zavalii, A.N. Sobolev, Dopov. Akad. Nauk Ukr. RSR, Ser. B 2 (1989) 37–39.
[13] S. Stein, L. Heletta, R. Pöttgen, Z. Naturforsch. 73b (2018) 765–772.
[14] J. Rodriguez-Carvajal, Physica B 192 (1993) 55–69, https://doi.org/10.1016/0921-4526(93)90108-I.
[15] J. Rodriguez-Carvajal, *basireps*: a computer program for calculating irreducible representations of little groups and basis functions of polar and axial vector properties, Available at: www.ill.eu/sites/fullprof/php/downloads.html.
[16] R. Harris, G.V. Raynor, J. Less Common Met. 9 (1965) 7–19.
[17] Ju B. Kuz'ma, V. Ja, Markiv, kristallografija SSSR 9, Sov. Phys. Crystallogr. 9 (1964) 279–280 (1964) 218.
[18] J.B. MacChesney, H.J. Williams, R.C. Sherwood, J.F. Potter, J. Appl. Phys. 37 (1966) 1435.
[19] J.B. MacChesney, H.J. Williams, R.C. Sherwood, J.F. Potter, J. Chem. Phys. 44 (1966) 596–601.
[20] R.M. Moon, W.C. Koehler, H.R. Child, L.J. Raubenheimer, Phys. Rev. 176 (1968) 722–731.
[21] E.F. Bertaut, J. Phys. Colloq. 32 (C1) (1971) 462–470, https://doi.org/10.1051/jphyscol:19711156.
[22] Yu A. Izyumov, V. Syromyatnikov, Phase Transitions and Crystal Symmetry, Kluwer Scademic Publishers, Dordrecht, 1990 (Chapter 2).
[23] Ł. Gondek, A. Szytuła, J. Alloys Compd. 442 (2007) 111–113.